Half-metallicity and structural properties of low-concentration Fe-doped SrS alloys: a first-principles study

S. Saleem [a], U. Parveen [a], H. AL- Ghamdi [b,*], M. Yaseen [a], I. Sajjad [a], Nasarullah [a]
[a] *Spin-Optoelectronics and Ferro-Thermoelectric (SOFT) Materials and Devices Laboratory, Department of Physics, University of Agriculture, Faisalabad 38040, Pakistan*
[b] *Department of Physics, College of Sciences, Princess Nourah bint Abdulrahman University, P. O. Box 84428, Riyadh 11671, Saudi Arabia*

Present research reveals the doping effect on physical properties of $Sr_{1-x}Fe_xS$ by employing ab-initio calculations. The negative formation energy and optimization outcomes exhibit the stability of the $Sr_{1-x}Fe_xS$ alloys with ferromagnetic phase. Spin dependent band structure (BS) and density of states (DOS) interpret that $Sr_{1-x}Fe_xS$ revealed half metallic ferromagnetic (HMF) nature at 6.25% and 12.5% of Fe doping while metallic character is revealed at 25% concentration of dopant. Spin-up state of $Sr_{0.9375}Fe_{0.0625}S$ and $Sr_{0.8750}Fe_{0.1250}S$ depicts semiconductive behavior with bandgap value of 2.01/2.33 eV, correspondingly, while metallic in spin-down channel. The magnetism in the system is mainly originated because of Fe-*d* state that further confirmed from magnetic spin density. The total magnetic moments are 4.001, 7.9889, 16.0180 (μ_B) for 6.25%, 12.5% and 25% doping, respectively. Furthermore, optical features are investigated to explore the role of concentration on the response of alloys to incident light (0-10 eV). The $\varepsilon_1(0)$ value are 13.4, 26.9, 70.1 for $Sr_{0.9375}Fe_{0.0625}S$, $Sr_{0.8750}Fe_{0.1250}S$ and $Sr_{0.75}Fe_{0.25}S$, respectively. The maximum absorption exists within of 3.4-7.89 eV for the studied compounds that make them suitable material for UV optoelectronic devices. Thus, the investigated alloys can be employed for spintronic and optical device usages.

(Received December 21, 2024; Accepted March 7, 2025)

Keywords: First principles calculations, Semiconductors, II-VI based alloys, Iron doped materials, Spintronics, Optical properties

1. Introduction

Spintronics and optoelectronics lead the way for improving modern technologies [1], aided by compact integrated circuits, nanometer-sized chips for storage information and well-ordered sensors [2-6]. Spintronics utilizes electrons spin states (up and down) in solid-state systems [7]. In spintronics, researchers are looking for appropriate materials to produce low-cost, small-size and high-speed electronic gadgets that exhibit asymmetric band dispersion above fermi level, known as half metallic ferromagnetic (HMF) and dilute magnetic semiconductors (DMSs). These would serve as spin diodes, valves and spin filters, whereas optoelectronics mainly relies on semiconductive materials [8-12]. These materials induces ferromagnetism (FM) by exchange coupling among *d*-electrons (transition metals (TM)) *s,* and *p* electrons from the host binary compound (semiconductor) to provide fascinating magneto-optical and magneto-transport features [13-15]. The spin of the host atoms is controlled by the TM atoms. HMF materials interpret the distinctive feature of being semiconductors in one spin direction and metallic in another, resulting 100% spin polarization near Fermi level (E_f)[16]. Consequently, in modern decades several researchers focused on exploring HMF in semiconductors (III-V, II-VI) for information storage chips[17-21]. HMF has been studied in innumerable materials, including perovskites compounds $La_{0.7}Sr_{0.3}MnO_3$ [22], double perovskites Sr_2FeMoO_6 [23] and in binary alloys such as Cr doped ZnTe/BeTe/BeSe, and V doped MgSe/Te, BeTe, ZnSe/Te [24-29].

* Corresponding author: hmalghmdi@pnu.edu.sa
https://doi.org/10.15251/CL.2025.223.223

The alkaline earth chalcogenides (II-VI, III-V) are important semiconductors having wide energy bandgap (E_g), low dielectric constants and valance band widths [30]. In this respect, the strontium sulfide (SrS) has engrossed scientific and industrial attention owing to its multiple technological applications in luminescent devices, catalysis, high resolution imaging, microelectronics[31-33]. SrS transformed from B1 to B2 phase at 18 GPa and its experimental lattice constant obtained for B1 structure (6.024 Å) [34]. Moreover, SrS consisted of flat valence band (generating a high DOS at valance's fringe) that formed a good candidate for ferromagnetism and easy to fabricate than other semiconductors owing to their chemical structure [35]. Recently, Fe doped binary compounds gained interest as ferromagnetic (FM) semiconductor owning to high high Curie temperature, suitability for high-speed spin gadgets, and low power consumption, prompting researchers to study their ferromagnetic mechanism [36]. Singh *et al*. investigated iron substitution in CdSe nanoparticles which resulted FM features at room-temperature and also increasing Fe concentration increased saturation magnetization [37]. The electromagnetic characteristics of Fe:CdS studied by Bourouis et al., found the strong half metallicity with robust hybridization among Fe-*d* and *p* -S orbitals [38]. Hamidane *et al.,* reported the $Sr_{1-x}Mn_xS$ and outcomes exposed that the lattice parameters decreased with increasing Mn concentration [39]. The solid phase reaction method was utilized to examine the optical and luminescence characteristics of Sm modified BaS, and found that direct and indirect excitation of Sm ions depended upon luminescence pattern [40]. Maurya *et al*., employed DFT to demonstrate HM behavior of Co, Fe, Ni modified barium sulfide and exposed that TMs-*d*/*p*-states played significant role in HM magnetism [41]. Furthermore, theoretical investigations were conducted to perceive HMF character in alike alloys such as Cr-modified MgSe/SrS, vanadium modified BaS, and SrO [42-44].

Herein, the physical characteristics of $Sr_{1-x}Fe_xS$ alloys are explored at different concentrations of Fe using DFT. Objective of the study is to formulate such compounds that have enhanced electromagnetic and optical features for innovative applications. Besides it, how impurity (Fe) atoms tune the studied features in SrS is also the focus of analysis. The results may lead to new routes to employ the investigated alloys in optoelectronics and spintronics gadgets.

2. Computational details

DFT is one of the most famous techniques for computing crystalline structure of the material, including electronic and optical properties, and other physical characteristics [45, 46]. The ground state structural parameters of titled alloys are estimated by optimizing and relaxing unit cell configurations. Computations were done by implementing FP-LAPW scheme of DFT as incorporated in the WIEN2k package [47]. It is one of the most suitable approach to solve Kohn Sham (KS) equations [48]. In cubic phase, exchange-correlation (XC) interactions were treated with PBEsol + GGA approximations. Each crystal unit-cell in the FP-LAPW method has two regions, an interstitial and a muffin-tin. A plane-wave orbit extends the potential in the earlier region, while the latter region consists of sphere-shaped harmonics [49].

$$V(r) = \begin{cases} \sum_{LM} Y_{LM}(\hat{r}) V_{LM}(r) & inner\ spher \\ \sum_K V_K E^{fK.r} & outer\ spher \end{cases} \quad (1)$$

For Sr, S, and Fe atoms, muffin tin radii (R_{MT}) are taken as 2.68, 2.15, and 1.52 (bohr), respectively. Inside the sphere, the angular momentum value is taken as $l_{max} = 10$. To control the plane wave expansion, the convergence parameter is set to $R_{MT} \times K_{max} = 10$. Here, R_{MT} elaborates the smallest value of muffin tin radii while K_{max} represents the highest value of reciprocal lattice. Using a mesh of 10x10x10, the Brillouin zone (BZ) integration is done using 1000 k-points. Sr, S and Fe have the respective valance electron configuration of $4s^2\ 4p^6\ 5s$, $2p^6\ 3s^2\ 3p^4$ and $3p^6\ 4s^2\ 3d^6$. Gaussian parameter, $G_{max} = 12$ is used for atomic radius conversion and energy cut-off parameter is set to -6.0 Ry to evade the charge leakage [50]. Furthermore, Kramers-Kronig (KK) relation is implemented to compute the dielectric constant of studied alloys [51, 52].

3. Results and discussions

3.1. Structural properties

Structure of any crystal have a major influence on its structural, electronic and optical characteristics [53]. The computation reveals that alloys have cubic crystal structure (see Fig. 1 (b, d, f)) belonging to $Fm\bar{3}m$ space group. In the unit cell, the Sr and S atom is placed at 4a (0, 0, 0) and 4b (0, ½, 0), respectively.

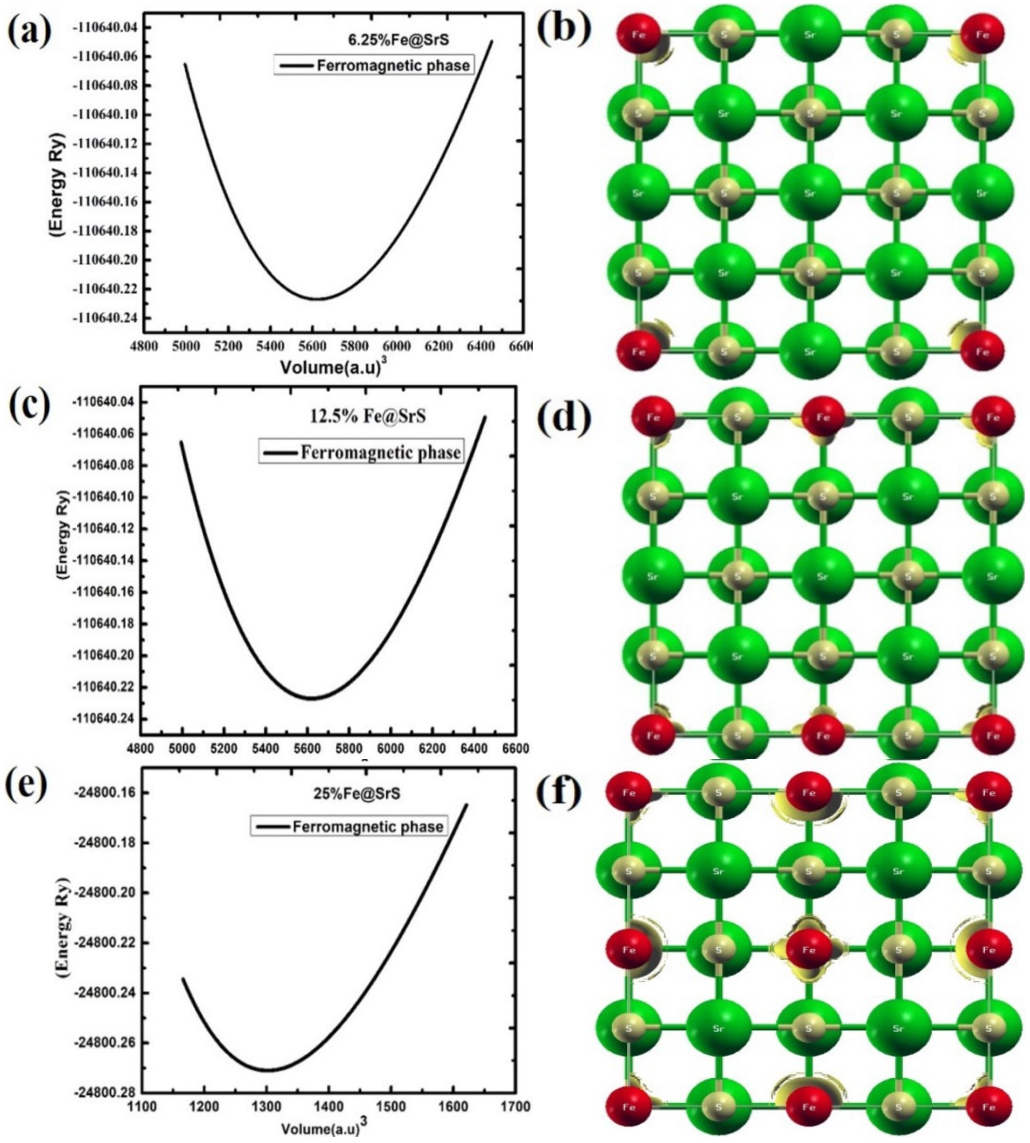

Fig. 1. Volume optimization and unit cells of ternary alloys $Sr_{1-x}Fe_xS$ at (a-b): $Sr_{0.9375}Fe_{0.0625}S$, (c-d): $Sr_{0.75}Fe_{0.25}S$, and (e-f): $Sr_{0.75}Fe_{0.25}S$.

By employing Birch-Murnaghan's equation of state (EOS), ground state energy of the system was computed [54, 55].

$$E(V) = E_0 + \frac{9B_0V_0}{16}\left[\left\{\left(\frac{V_0}{V}\right)^{\frac{2}{3}} - 1\right\}^2 2\left\{3 - 2\left(\frac{V_0}{V}\right)^{\frac{2}{3}}\right\} + \left\{\left(\frac{V_0}{V}\right)^{\frac{2}{3}} - 1\right\}^3 B'_0\right] \quad (2)$$

Energy versus volume (E-V) curve is drawn that interprets the firmness of the studied alloys in ferromagnetic phase (see Fig. 1(a, c, e)). After fitting data with EOS, the optimized structural parameters that include lattice constant (a_o), ground state energy (E_o), optimized volume (V_o), bulk modulus (B_o) and its pressure derivative (B') are computed (see Table 1). There is slight increase in lattice constant values as the dopant concentration increases owing to the increased ionic radii of Fe contrary to Sr. Furthermore, during structure optimization, Fe atoms move away from Sr as the dopant concentration increases that resulted in increased value of a_o at 25% Fe-concentration [56-58]. It is evident that the B_o has smaller value at 6.25% doping concentration with relative to 25%. It interprets that $Sr_{0.9375}Fe_{0.0625}S$ is more compressible. Increased B_o value illustrates structural rigidity that is the significant aspect for spintronic applications [59, 60].

Additionally, to investigate the thermodynamic firmness of alloys, enthalpy of formation energy (ΔH_f) is computed by utilizing following relation:

$$\Delta H_f = E_{tot}(Sr_{1-x}Fe_xS) - aE_{Fe} - bE_{Sr} - cE_S \quad (3)$$

In above relation, E_{tot} is the total energy of the alloys, while E_{Fe}, E_S and E_{Sr} display the formation energy of the individual Fe, Sr and S atoms [61]. Number of atoms in a unit cell is displayed through a, b and c. The results expose negative ΔH_f values (see Table 1) that confirms the firmness of alloys [62]. It further reveals that the reaction would be exothermic when the studied alloys are synthesized.

Table 1. Enthalpy of formation energies and ground state features for $Sr_{1-x}Fe_xS$ alloys.

Structural Parameters	Concentration of Fe atoms		
	$Sr_{0.9375}Fe_{0.0625}S$	**$Sr_{0.875}Fe_{0.125}S$**	**$Sr_{0.75}Fe_{0.25}S$**
a_o (Bohr)	10.0856	10.1392	10.2179
V_o (a.u)^3	5620.8543	2743.6033	1301.4369
E_o (Ryd.)	-110640.226955	-53413.582629	-24800.271021
B_o (GPa)	54.6031	57.6646	60.9958
B_o'	4.5353	5.1167	5.1394
ΔH_f (eV)	-2.12	-2.34	- 2.48

3.2. Electronic features

In order to achieve a good comprehension related to electronic behavior of studied alloys, electronic properties are computed [63]. These features of the system is evaluated from BS and DOS to expose the nature (semiconductor, half metallic, metallic, insulator) of the alloys [64]. BS is further useful for revealing the orbital contribution in electronic properties. The electron diffraction in periodic crystal lattices resulted the formation of bands in solids [65]. Energy structure of the compounds depends on orbital interactions in lattices. In literature, it is found that the intrinsic SrS executes semiconductor nature with bandgap (E_g) value of 2.5 eV [35]. After Fe doping, the SrS alloys are polarized in (up/down) spin versions at different concentrations and induces magnetism in system. $Sr_{1-x}Fe_xS$ (x= 6.25%, 12.5%) revealed the semiconductive nature in up-spin channel (left pannel) with E_g value of 2.01, 2.33 eV, while metallic nature in down-spin (right pannel) state; revealing HMF nature that leads to 100% spin polarized states (see Fig. 2 (a, c, d, f)). E_g value in up-spin channel reduces due to upward shifting of valance band (VB) through incrementing concentration of impurity atom and exposed metallic character in both spin channels for $Sr_{0.75}Fe_{0.25}S$ alloys (see Fig. 2 (g, i)).

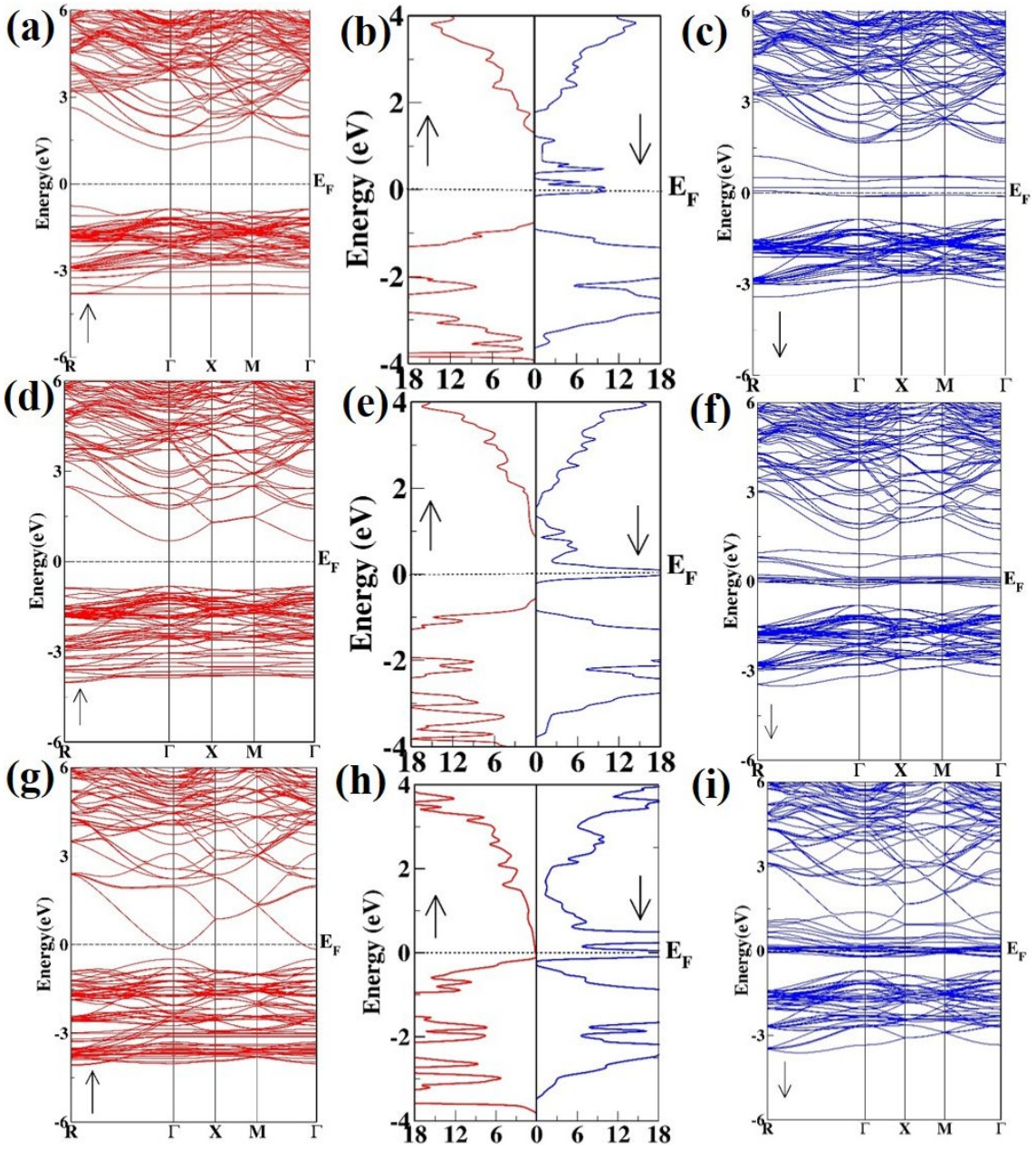

Fig. 2. Band structure plots (left and right section) and total density of state plots (central section) of (a-c) $Sr_{0.9375}Fe_{0.0625}S$ (d-f) $Sr_{0.8750}Fe_{0.1250}S$ (g-i) $Sr_{0.750}Fe_{0.250}S$.

In addition to band structure analysis, the qualitative explanation for VB, conduction band (CB) and the energy states are exposed by DOS (total DOS and partial DOS). TDOS spectra (see Fig. 2 (b, e, h))) reveals similar scenario as observed in BS and displays how different states affect the band arrangement. To investigate the origination of hybridization and magnetic moments of $Sr_{1-x}Fe_xS$ alloy, PDOS is investigated (see Fig. 3(a-i)). It allows assessing the participation of each atom to the crystal structure. The VB is majorly consisted of Fe-*d* and *p*-S orbitals in both spin states of band formation. The participation of states around fermi level (E_f) were found -0.1 to 0 eV (dn-spin) and -0.2-0 eV (up-spin) as shown in Fig. 3(a-f). For 6.25% and 12.5% concentrations, the CB is mainly populated from Fe-*d* state within range of 2.43-6 eV with minor participation of Sr-*s/p* orbitals. The hybridization exists between Fe-*d* and S-*p* states from 2.5 to 5.1 eV (See Fig. 3 a, d, c, f). The dominant peaks of Fe-*d/s* and S-*p* orbitals with minor involvement of Sr-p/d and S-s states, however in CB region curves of Fe-d and S-p are dominant (see Fig. 3 (g, h, i)).

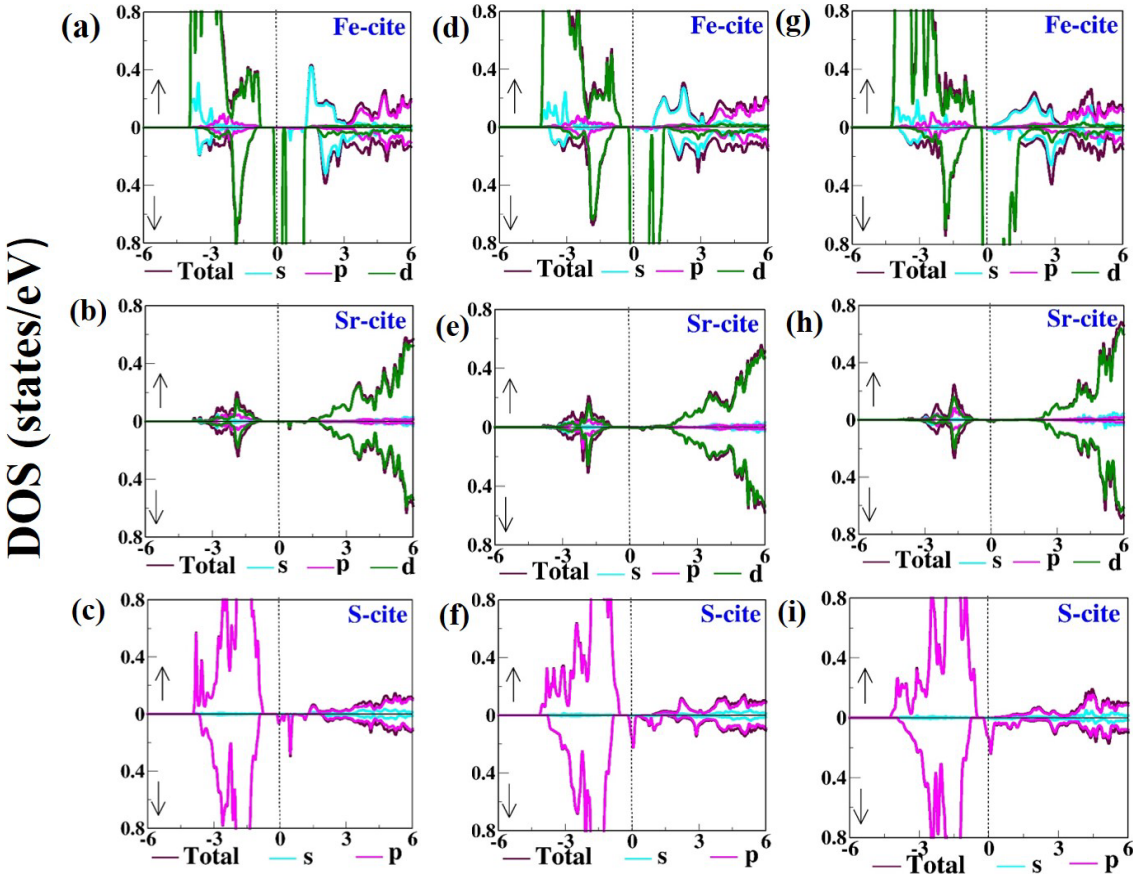

Fig. 3. Partial DOS of (a-c) $Sr_{0.9375}Fe_{0.0625}S$ (d-f) $Sr_{0.8750}Fe_{0.1250}S$ (g-i) $Sr_{0.750}Fe_{0.250}S$.

3.3. Magnetic features

The magnetic character of $Sr_{1-x}Fe_xS$ (x= 6.25%, 12.5%, 25%) are examined to calculate the interstitial, total and local magnetic moments (μ_B) (see Table 2).

Table 2. Computed magnetic moment (μ_B) of $Sr_{1-x}Fe_xS$ alloys.

Alloys	Magnetic Moment (μ_B)				
	Total	Interstitial	Fe	Sr	S
$Sr_{0.9375}Fe_{0.0625}S$	4.0018	0.13671	3.59317	0.00429	0.12483
$Sr_{0.875}Fe_{0.125}S$	7.9889	0.25579	7.2015	0.00743	0.35642
$Sr_{0.75}Fe_{0.25}S$	16.0180	0.51321	14.41905	-0.00073	3.07463

The total magnetic moment (M_{Tot}) in a cell is 4.0018, 7.9889, 16.0180 μ_B for 6.25%, 12.5% and 25% doping concentrations, respectively. Magnetism increased with increasing doping content, which confirm the FM character that based on Hund's rule [66]. The Fe-d state is the base for the enhanced magnetic moment in studied compounds that is confirmed through magnetic densities (see Fig. 1b, d, f), while the minor magnetization originates from hybridization of nonmagnetic Sr-s and S-p orbitals. Furthermore, the spin alignment of each atom of corresponding compound is designated by negative and positive values of μ_B.. Magnetic moments with positive signs indicates the alignment of spins in the identical direction, while negative sign indicates opposite spin alignment, indicating ferrimagnetic/anti-FM features [67].

3.4. Optical features

Optical characteristics are essential to analyze the feature of a alloys when electromagnetic radiations fall on it. To explore the prospective optoelectronic applications of a compound, a comprehensive insight regarding its response to ultraviolet (UV), visible and infrared energy range is necessary [68, 69]. The optical analysis of $Sr_{0.9375}Fe_{0.0625}S$, $Sr_{0.8750}Fe_{0.1250}S$ and $Sr_{0.750}Fe_{0.250}S$ including the study of absorption coefficient, and optical conductivity are examined. In optoelectronic devices, light absorption and emission depend on inter-band and intra-band transitions [70]. Inter-band transitions play significant role in semiconductors, but in metals, intra-band transitions are important [71]. Dielectric function (ε(ω)) is directly linked to BS and reveals that how an optically active material responds to incident energy (E=hf) [65]. The ε(ω) is represented by:

$$\varepsilon(\omega) = \varepsilon_1(\omega) + i\varepsilon_2(\omega) \tag{4}$$

Here, real part $\varepsilon_1(\omega)$ defines the polarization/dispersion of light, while imaginary part $\varepsilon_2(\omega)$ illustrates the absorptive behavior of light [72, 73]. Using Kramer's Kronig model, the $\varepsilon_1(\omega)$ and $\varepsilon_2(\omega)$ can be computed as given below [74]:

$$\varepsilon_1(\omega) = 1 + \frac{2}{\pi} p \int_0^{\Theta} \frac{\omega'(\varepsilon_2(\omega'))}{\omega'^2 - \omega^2} d\omega' \tag{5}$$

$$\varepsilon_2(\omega) = \frac{e^2\hbar}{\pi m^2 \omega^2} \sum_{vc} \int |n, n'(k,q)|^2 [\omega n, n'(k) - \omega] \, d^3k \tag{6}$$

For $Sr_{0.9375}Fe_{0.0625}S$, $Sr_{0.8750}Fe_{0.1250}S$ and $Sr_{0.750}Fe_{0.250}S$, the static dielectric function $\varepsilon_1(0)$ values are 13.4, 26.9, 70.1, respectively (see Table 3). It interprets that with increasing concentration of Fe atoms polarization increases. E_g and $\varepsilon_1(0)$ have inverse relation, as stated by Penn's model [75].

$$\varepsilon_1(0) \approx (\omega_p / E_g)^2 \tag{7}$$

With increase in energy, its value decreases, but after 7.1 eV, its value becomes constant (See Fig. 4a). Similar compounds are being investigated by a number of researchers. Cr doped BeSe have values ($\varepsilon_1(0)$) of 6.5, 21.8, 28.1, 80.7, 58.1 at 6.25%, 12.5%, 18.75%, 25% concentrations, respectively [76]. $Cd_{1-x}CoX$ (X= Te, S, Se) have ($\varepsilon_1(0)$) values of 25.67, 70.50 and 59.67, respectively [77]. At 25% doping concentration, $\varepsilon_1(0)$ has negative values at 7.4 eV exposing the metallic behavior of the system [78].

In the optical spectra of a compound, $\varepsilon_2(\omega)$ plays a significant role and illustrates the absorption capacity. It further reveals the information about threshold energy points of a material, which correspond to electronic transitions between unoccupied and occupied states [79]. The optical critical points for $Sr_{1-x}Fe_xS$ (x= 6.25%, 12.5%, 25%), occurs at 0.2-2.9 eV (see Fig. 4b). The studied material is more absorbent between 4.5-7.0 eV (UV zone) that exemplify the studied material is suitable for optical devices. Energy variance is mainly caused by differences in E_g of system at different concentrations.

Absorption coefficient (α (ω)) illustrates the decrease in light intensity as it propagates through a material (see Fig. 4c) [80]. The absorption spectra is associated with $\varepsilon_2(\omega)$ as given in the equation [81]:

$$\alpha(\omega)_j = \frac{\omega}{c} \sqrt{2\left[\left|\varepsilon(\omega)_j\right| - Re(\varepsilon(\omega)_j)\right]} \tag{8}$$

With Fe doping, the width of the absorption zone upsurges. Furthermore, the maximum peak is shifted towards high energy, reflecting the blue-shift analogous to $\varepsilon_2(\omega)$ graph. For the studied materials, the first maximum magnitude of peaks lies within 3.4-7.89 eV, representing the UV zone. Thus, the light dispersion is minimum in the stated region. Another little peak is also observed at 9 eV with the value of 147×10^4 cm^{-1} for 6.25% and 12.5% dopant concentrations, indicating the

absorption at this energy. In case of 25% Fe-concentration, maximum value of α (ω) is 130×10^4 cm^{-1} at 7.89 eV. These results quantify that in UV zone, absorption intensity of peaks decreases via increasing concentrations of dopant atoms.

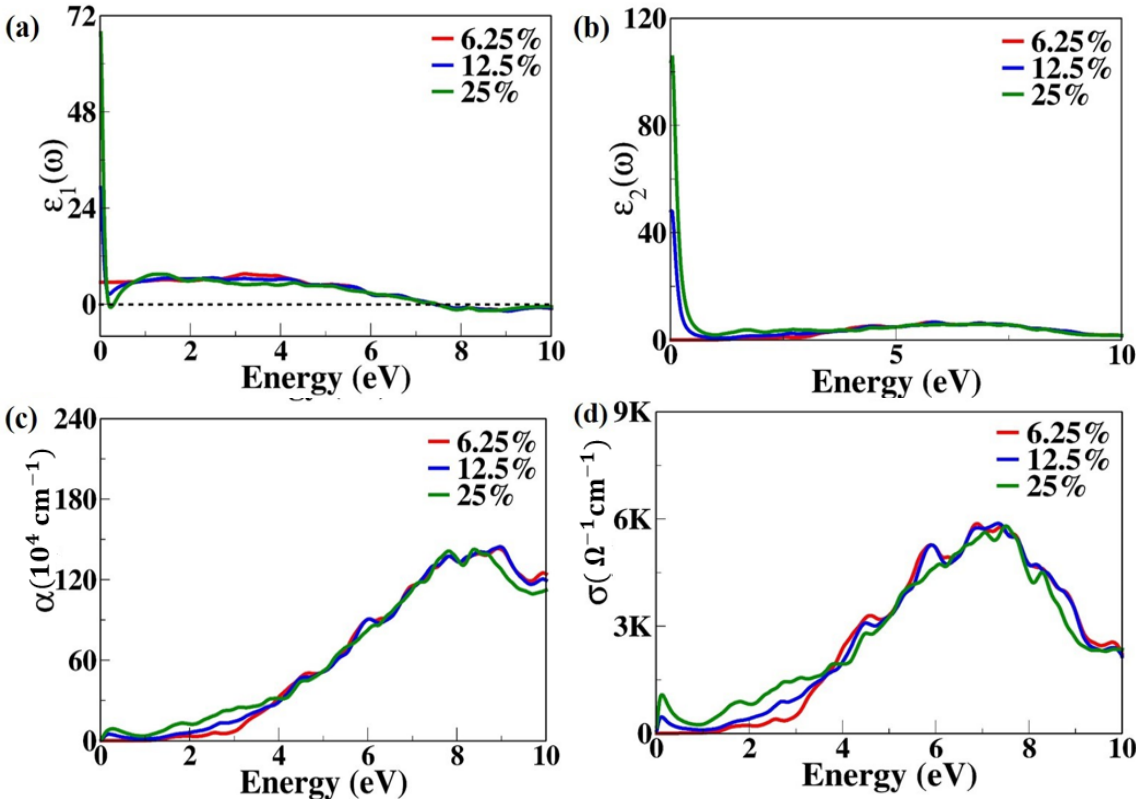

Fig. 4. (a) $\varepsilon_1(\omega)$, (b) $\varepsilon_2(\omega)$, (c) $\alpha(\omega)$, and (d) $\sigma(\omega)$.

Absorbing photon energy resulted inter-band electronic excitations that contributes to the conductivity of the system. It is known as optical conductivity σ(ω) that has similar characteristic features as ε2(ω). It also depends upon inter and intra band transitions and interprets the photoconductivity of the material. The maximum α (ω) leads to higher σ(ω), represents that the energy photons need more energy to break bonds. Its peak values lie within 4.2-7.5 eV energy limit and then declined trend is observed (see Fig. 4d). At maxima of conductivity, $\varepsilon_1(\omega)$ is negative (see Fig. 4a) that illustrates the maximum conductivity is in metallic zone. The highest σ(ω) values are 5864(at 6.83), 5852 (at 7.3) and 5739 $\Omega^{-1}cm^{-1}$ (at 7.5 eV) for $Sr_{0.9375}Fe_{0.0625}S$, $Sr_{0.8750}Fe_{0.1250}S$ and $Sr_{0.750}Fe_{0.250}S$, respectively.

Another significant parameter is complex refractive index that mathematically expressed in the following way [82]:

$$\tilde{n}(\omega) = n\,(\omega) + ik\,(\omega) \tag{9}$$

n(ω) depicts the light propagation through a material. Complex refractive index of a compound can be computed through [83]

$$n(\omega) = \frac{1}{\sqrt{2}}\left[\sqrt{{\varepsilon_1}^2(\omega) + {\varepsilon_2}^2(\omega)} + \varepsilon_1(\omega)\right]^{1/2} \tag{10}$$

$$k(\omega) = \frac{1}{\sqrt{2}}\left[\sqrt{{\varepsilon_1}^2(\omega) + {\varepsilon_2}^2(\omega)} - \varepsilon_1(\omega)\right]^{1/2} \tag{11}$$

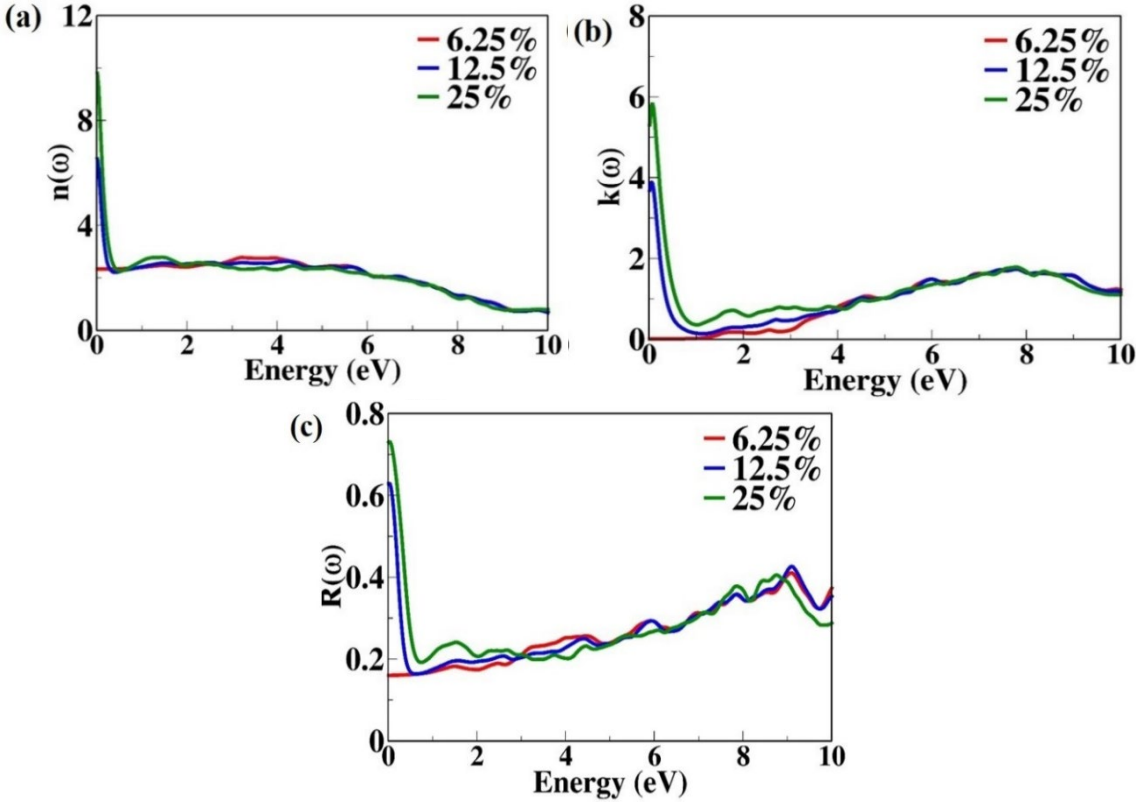

Fig. 5. (a) n(ω), (b) k(ω), and (c) R(ω).

Static values of n(0) are 2.6, 7.2, 9.8 for $Sr_{0.9375}Fe_{0.0625}S$, $Sr_{0.8750}Fe_{0.1250}S$ and $Sr_{0.750}Fe_{0.250}S$, respectively (see Table 3). For comparison with reported literature, $Ba_{1-x}Mn_xS$ (x= 6.25%, 12.5%, 25%) alloys revealed n(0) values of 2.3, 2.4, 2.5, respectively [70] and for $Be_{1-x}Cr_xSe$ (x= 6.25%, 12.5%, 18.75%, 25%), exposed n(0) values of 4.8, 5.3, 9.2 and 7.7, respectively [76]. In the studied doped compounds, the static n(ω) values upsurge via increasing doping content (see Fig. 5a). Its maximum values appeared at 4.2 eV (in UV zone) owing to electronic transition from VB to CB then decline to lower values of n(ω) at higher energy limit. It is because, the direct electronic de-excitation at high energy limit is not possible, hence, energy is dissipated [84]. k(ω) measures the photons reduction in a system owing to scattering and absorption [85]. Extinction coefficient k(ω) assessed through ε(ω) by the following relations [86]:

$$\varepsilon_2(\omega) = 2nk \tag{12}$$

$$\varepsilon_1(\omega) = n^2 - k^2 \tag{13}$$

It is directly associated with absorption and $\varepsilon_2(\omega)$as represented by the equation [87].

$$k(\omega) = \frac{\lambda \alpha(\omega)}{4\pi} \tag{14}$$

The peaks range of k(ω) occur within visible to UV zone (see Fig. 5b). For all under discussing concentration of Fe ions, it is observed that the highest value of k(ω) is 1.8 at 7.8 eV.

Reflectivity R(ω) examines the surface nature of the system. It further elaborates the ratio of reflected to the incident light [60]. Mathematically, it is expressed as: [83]

$$R(\omega) = \frac{k^2(\omega)+(n(\omega)-1)^2}{k^2(\omega)+(n(\omega)+1)^2} \tag{15}$$

Maximum R(ω) occurs at the energy range where $\varepsilon_1(\omega)$ values become negative. Initially, the reflectivity was 18 % (0.18), 62 % (0.62) and 73 % (0.73) for $Sr_{0.9375}Fe_{0.0625}S$, $Sr_{0.8750}Fe_{0.1250}S$ and $Sr_{0.750}Fe_{0.250}S$, correspondingly (see Table 3) owing to lattice vibrations in the system [76]. The R(ω) spectra reveal that its value is small at low energy while the reflectivity elevates at intermediate and high energies (see Fig. 5c). The highest R(ω) values are 43%, 42% and 40% at 9.2, 9.2 and 8.76 eV for $Sr_{0.9375}Fe_{0.0625}S$, $Sr_{0.8750}Fe_{0.1250}S$ and $Sr_{0.750}Fe_{0.250}S$, respectively.

Table 3. Calculated $\mathcal{E}_1(0)$, n(0), R(0) and E_g of $Sr_{1-x}Fe_xS$ alloys.

Alloys	E_g (eV)		$\mathcal{E}_1(0)$	n(0)	R(0)
	Spin-up	Spin-down			
$Sr_{0.9375}Fe_{0.0625}S$	2.01	0	13.4	2.6	0.18
$Sr_{0.875}Fe_{0.125}S$	2.33	0	26.9	7.2	0.62
$Sr_{0.75}Fe_{0.25}S$	0	0	70.1	9.8	0.73

4. Conclusion

Herein, the spin dependent DFT examination is executed to explore the electromagnetic, structural and optical characteristics of $Sr_{1-x}Fe_xS$ alloys. The calculations are performed by employing FP-LAPW scheme as implemented in WIEN2k code. Firmness of $Sr_{1-x}Fe_xS$ is ensured by the negative enthalpy of formation energy. At 6.25% and 12.5% of Fe concentration, spin polarized electronic BS and DOS reveals the HMF nature and exposed metallic character at 25% doping concentration. Computed values of the M_{Tot} μ_B for $Sr_{0.9375}Fe_{0.0625}S$, $Sr_{0.8750}Fe_{0.1250}S$ and $Sr_{0.750}Fe_{0.250}S$ are 4.0018, 7.9889, 16.0180 μ_B, respectively that mainly comes from Fe-*d* state. The optical features are examined within 0-10 eV. The studied doped compounds have maximum absorption and conductivity in UV zone. Overall analysis suggests that the $Sr_{1-x}Fe_xS$ is a promising alloys for spintronic and optoelectronic devices.

Acknowledgements

This research project was funded by the Deanship of Scientific Research and Libraries, Princess Nourah bint Abdulrahman University, through the Program of Research Project Funding After Publication, grant No (RPFAP-27-1445).

References

[1] Tariq, Z., et al., Vanadium based zinc spinel oxides: Potential materials as photoanode for water oxidation and optoelectronic devices. 2021. 46(55): p. 28110-28120; https://doi.org/10.1016/j.ijhydene.2021.06.073

[2] Felser, C., G.H. Fecher, and B.J.A.C.I.E. Balke, Spintronics: a challenge for materials science and solid-state chemistry. 2007. 46(5): p. 668-699; https://doi.org/10.1002/anie.200601815

[3] Haider, A., et al., Investigation of Mg1− xNixS Alloys for Spintronic and Optoelectronic Application. p. 2400375; https://doi.org/10.1002/pssb.202400375

[4] Ali, M.A., et al., Insight into pressure tunable structural, electronic and optical properties of CsYbF3 via DFT calculations. 2020. 135(3): p. 309; https://doi.org/10.1140/epjp/s13360-020-00325-8

[5] Ali, M.A., et al., Modeling of structural, elastic, mechanical, acoustical, electronic and thermodynamic properties of XPdF3 (X= Rb, Tl) perovskites through density functional theory. 2020. 95(7): p. 075705; https://doi.org/10.1088/1402-4896/ab8eee

[6] Ullah, R., et al., Influence of the spin-orbit coupling effect on the electronic and thermoelectric properties of Cs2MI6 (M= Zr, Hf) variant perovskites. 2021. 134: p. 111112; https://doi.org/10.1016/j.materresbull.2020.111112

[7] Bowen, M., 13 - Spintronics: An application of complex metal oxides, in Epitaxial Growth of Complex Metal Oxides, G. Koster, M. Huijben, and G. Rijnders, Editors. 2015, Woodhead Publishing. p. 365-395; https://doi.org/10.1016/B978-0-08-102945-9.00009-5

[8] Žutić, I., J. Fabian, and S.D.J.R.o.m.p. Sarma, Spintronics: Fundamentals and applications. 2004. 76(2): p. 323; https://doi.org/10.1103/RevModPhys.76.323

[9] Coey, J., M.J.J.o.A.P. Venkatesan, Half-metallic ferromagnetism: Example of CrO2. 2002. 91(10): p. 8345-8350; https://doi.org/10.1063/1.1447879

[10] Santos-Carballal, D., et al., First-principles study of the inversion thermodynamics and electronic structure of Fe M 2 X 4 (thio) spinels (M= Cr, Mn, Co, Ni; X= O, S). 2015. 91(19): p. 195106; https://doi.org/10.1103/PhysRevB.91.195106

[11] Saleem, S., et al., Thermodynamical stability and optoelectronic characteristics of Sr1-xCoxTe: A DFT study. 2024. 692: p. 416378; https://doi.org/10.1016/j.physb.2024.416378

[12] Saha, D., et al., 6.15 - Spin-Based Semiconductor Heterostructure Devices, in Comprehensive Semiconductor Science and Technology, P. Bhattacharya, R. Fornari, and H. Kamimura, Editors. 2011, Elsevier: Amsterdam. p. 563-614; https://doi.org/10.1016/B978-0-44-453153-7.00042-0

[13] Furdyna, J.K.J.J.o.A.P., Diluted magnetic semiconductors. 1988. 64(4): p. R29-R64; https://doi.org/10.1063/1.341700

[14] Zou, S., et al., Bosonic lasing from collective exciton magnetic polarons in diluted magnetic nanowires and nanobelts. 2016. 3(10): p. 1809-1817; https://doi.org/10.1021/acsphotonics.6b00289

[15] Katayama-Yoshida, H., K.J.J.o.P. Sato, and C.o. Solids, Spin and charge control method of ternary II-VI and III-V magnetic semiconductors for spintronics: Theory vs. experiment. 2003. 64(9-10): p. 1447-1452; https://doi.org/10.1016/S0022-3697(03)00126-4

[16] Katsnelson, M., et al., Half-metallic ferromagnets: From band structure to many-body effects. 2008. 80(2): p. 315-378; https://doi.org/10.1103/RevModPhys.80.315

[17] Rajamanickam, N., et al., Effect of Mn-doping on the structural, morphological and optical properties of ZnO nanorods. 2014. 65: p. 240-247; https://doi.org/10.1016/j.spmi.2013.11.005

[18] Rajendar, V., et al., Systematic approach on the fabrication of Co doped ZnO semiconducting nanoparticles by mixture of fuel approach for Antibacterial applications. 2014. 75: p. 551-563; https://doi.org/10.1016/j.spmi.2014.07.049

[19] Kaur, P., et al., Investigations on doping induced changes in structural, electronic structure and magnetic behavior of spintronic Cr-ZnS nanoparticles. 2015. 83: p. 785-795; https://doi.org/10.1016/j.spmi.2015.04.016

[20] Doumi, B., et al., First-principle investigation of magnetic and electronic properties of vanadium-and chromium-doped cubic aluminum phosphide. 2015. 32: p. 166-171; https://doi.org/10.1016/j.mssp.2015.01.014

[21] Xiao, W.-Z., Meng, B., Xu, H.-Q., Chen, Q. and Wang, L.-L. (2016), Electronic and magnetic properties in Mn-doped IIIA-nitride monolayers. 253: 2001-2008; https://doi.org/10.1002/pssb.201552761

[22] Soulen Jr, R., et al., Measuring the spin polarization of a metal with a superconducting point contact. 1998. 282(5386): p. 85-88; https://doi.org/10.1126/science.282.5386.85

[23] Kobayashi, K.-I., et al., Room-temperature magnetoresistance in an oxide material with an ordered double-perovskite structure. 1998. 395(6703): p. 677-80; https://doi.org/10.1038/27167

[24] Saito, H., et al., Room-temperature ferromagnetism in highly Cr-doped II-VI diluted magnetic semiconductor Zn 1− x Cr x Te. 2003. 93(10): p. 6796-6798; https://doi.org/10.1063/1.1556117

[25] Picozzi, S., et al., First-principles prediction of half-metallic ferromagnetic semiconductors: V-and Cr-doped BeTe. 2003. 67(16): p. 165203; https://doi.org/10.1103/PhysRevB.67.165203

[26] Sajjad, M., et al., Theoretical investigation of structural, electronic, and magnetic properties of V-doped MgSe and MgTe semiconductors. 2014. 27: p. 2327-2336; https://doi.org/10.1007/s10948-014-2593-1

[27] Monir, M.E.A., et al., Density functional theory investigation of half-metallic ferromagnetism in V-doped GaP alloys. 2020. 497: p. 166067; https://doi.org/10.1016/j.jmmm.2019.166067

[28] Monir, M.E.A., et al., First-principles calculations of a half-metallic ferromagnet zinc blende Zn1− xVxTe. 2015. 378: p. 41-49; https://doi.org/10.1016/j.jmmm.2014.10.070

[29] Monir, M.E.A., et al., Spin-polarized structural, elastic, electronic and magnetic properties of half-metallic ferromagnetism in V-doped ZnSe. 2015. 374: p. 50-60; https://doi.org/10.1016/j.jmmm.2014.08.014

[30] Ruoff, A. and T.J.T.S. Grzybowski, Tokyo, Solid state physics under pressure. 1985; https://doi.org/10.1103/PhysRevB.27.6502

[31] Pandey, R., S.J.J.o.P. Sivaraman, and C.o. Solids, Spectroscopic properties of defects in alkaline-earth sulfides. 1991. 52(1): p. 211-225; https://doi.org/10.1016/0022-3697(91)90066-9

[32] Yamashita, N., et al., Luminescence of Pb2+ centers in SrS and SrSe phosphors. 1984. 53(1): p. 419-426; https://doi.org/10.1143/JPSJ.53.419

[33] Varshney, D., et al., High pressure structural (B1-B2) phase transition and elastic properties of II-VI semiconducting Sr chalcogens. 2008. 41(4): p. 529-537; https://doi.org/10.1016/j.commatsci.2007.05.009

[34] Syassen, K.J.P.S.S.A., Applied Research, Pressure-induced structural transition in SrS. 1985. 91(1): p. 11-15; https://doi.org/10.1002/pssa.2210910102

[35] Yari, A., A. Boochani, and S.J.C.P. Rezaee, Electronic, optical, magneto-optical, and thermoelectric properties of the SrS graphene-like under Cr impurity. 2021. 551: p. 111355; https://doi.org/10.1016/j.chemphys.2021.111355

[36] Shinya, H., et al., First-principles prediction of the control of magnetic properties in Fe-doped GaSb and InSb. 2018. 124(10); https://doi.org/10.1063/1.5046912

[37] Singh, J., N.J.J.o.s. Verma, and n. magnetism, Synthesis and characterization of Fe-doped CdSe nanoparticles as dilute magnetic semiconductor. 2012. 25: p. 2425-2430; https://doi.org/10.1007/s10948-012-1631-0

[38] Bourouis, C., A.J.J.o.m. Meddour, and m. materials, First-principles study of structural, electronic and magnetic properties in Cd1− xFexS diluted magnetic semiconductors. 2012. 324(6): p. 1040-1045; https://doi.org/10.1016/j.jmmm.2011.10.022

[39] Hamidane, N., et al., First-principles investigation of the structural, electronic, magnetic, thermodynamic and optical properties of the cubic Sr1-xMnxS ternary alloys. 2020. 23: p. e00458; https://doi.org/10.1016/j.cocom.2020.e00458

[40] Maeda, K., et al., X-ray and photoluminescence properties of Sm3+ doped barium sulfide. 2012. 9(12): p. 2271-2274; https://doi.org/10.1002/pssc.201200321

[41] Maurya, S., R. Sharma, K. Bhamu, AIP Conference Proceedings. 2018. AIP Publishing; https://doi.org/10.1063/1.5029043

[42] Ambreen, H., et al., First principle insight on physical characteristics of Mn doped BeS compound. 2021. 127: p. 105697; https://doi.org/10.1016/j.mssp.2021.105697

[43] Berber, M., et al., First-principle predictions of electronic properties and half-metallic ferromagnetism in vanadium-doped rock-salt SrO. 2018. 47: p. 449-456; https://doi.org/10.1007/s11664-017-5793-1

[44] Addadi, Z., et al., Electronic and ferromagnetic properties of 3 d (V)-doped (BaS) barium sulfide. 2017. 30: p. 917-923; https://doi.org/10.1007/s10948-016-3894-3

[45] Van Mourik, T., M. Bühl, and M.-P. Gaigeot, Density functional theory across chemistry, physics and biology. 2014, The Royal Society Publishing. p. 20120488; https://doi.org/10.1098/rsta.2012.0488

[46] Kohn, W., A.D. Becke, and R.G. Parr, Density functional theory of electronic structure. The journal of physical chemistry, 1996. 100(31): p. 12974-12980; https://doi.org/10.1021/jp960669l

[47] Blaha, P., et al., WIEN2k: An APW+ lo program for calculating the properties of solids. The Journal of chemical physics, 2020. 152(7); https://doi.org/10.1063/1.5143061

[48] Gous, M., A. Meddour, and C. Bourouis, First principles study of structural, electronic, magnetic and elastic properties of Mg0. 75TM0. 25S (TM= Mn, Fe, Co, Ni)., 2017. 422: p. 271-279; https://doi.org/10.1016/j.jmmm.2016.09.001

[49] Elhag, A.J.R.i.P., DFT study on the crystal, electronic and magnetic structures of tantalum based double perovskite oxides Ba2MTaO6 (M= Cr, Mn, Fe) via GGA and GGA+ U. 2018. 9: p. 793-805; https://doi.org/10.1016/j.rinp.2018.03.055

[50] Shoukat, L., et al., Tuned physical characteristics of PbSe binary compound: a DFT study. 2022. 18(5); https://doi.org/10.15251/JOR.2022.185.649

[51] Ghazanfar, M., et al., Journal of Solid State Chemistry, 2021. 301: p. 122335; https://doi.org/10.1016/j.jssc.2021.122335

[52] Lucarini, V., et al., Kramers-Kronig relations in optical materials research. Vol. 110. 2005: Springer Science & Business Media; https://doi.org/10.1007/b138913

[53] Najrin, F., et al., Results in Materials, 2024. 23: p. 100610; https://doi.org/10.1016/j.rinma.2024.100610

[54] Blaha, P., et al., wien2k. 2001. 60(1); https://doi.org/10.1016/S0927-0256(03)00112-5

[55] Ahmed, R., et al., Computational Materials Science, 2007. 39(3): p. 580-586; https://doi.org/10.1016/j.commatsci.2006.08.014

[56] Doumi, B., et al., FThe European Physical Journal B, 2015. 88: p. 1-9; https://doi.org/10.1140/epjb/e2015-50746-9

[57] Khan, M.S., et al., Materials Science in Semiconductor Processing, 2022. 150: p. 106965; https://doi.org/10.1016/j.mssp.2022.106965

[58] Poonam, P., H.S. Saini, M.K. Kashyap, AIP Conference Proceedings. 2020. AIP Publishing; https://doi.org/10.1063/5.0017730

[59] Bhojani, A.K., H.R. Soni, P.K. Jha, AIP Advances, 2020. 10(1); https://doi.org/10.1063/1.5121832

[60] Afzal, F., et al., Physica B: Condensed Matter, 2025. 696: p. 416631; https://doi.org/10.1016/j.physb.2024.416631

[61] Saleem, S., et al., Physica Scripta, 2022. 97(9): p. 095817; https://doi.org/10.1088/1402-4896/ac8a27

[62] Mahmood, Q., et al., Solid State Communications, 2019. 299: p. 113654; https://doi.org/10.1016/j.ssc.2019.113654

[63] Zoubir, M.H., et al., Revista Mexicana de Física, 2024. 70(2 Mar-Apr): p. 020501 1-9-020501 1-9; https://doi.org/10.31349/RevMexFis.70.020501

[64] Saleem, S., et al., Exploring the Mn doped BaTe alloy for spintronics and energy harvesting applications. 2024. 99(6): p. 065965; https://doi.org/10.1088/1402-4896/ad41a0

[65] Chattopadhyaya, S., R.J.J.o.P. Bhattacharjee, C.o. Solids, FP-LAPW methodology based theoretical investigation of structural, electronic and optical properties of MgxPb1− xS, MgxPb1− xSe and MgxPb1− xTe ternary alloys. 2017. 100: p. 57-70; https://doi.org/10.1016/j.jpcs.2016.09.005

[66] Murtaza, G., et al., Structural, chemical bonding, electronic and magnetic properties of KMF3 (M= Mn, Fe, Co, Ni) compounds. 2014. 85: p. 402-408; https://doi.org/10.1016/j.commatsci.2013.12.054

[67] Addadi, Z., et al., Journal of Superconductivity and Novel Magnetism, 2017. 30: p. 917-923; https://doi.org/10.1007/s10948-016-3894-3

[68] Ahmed, R., et al., Journal of Materials Research and Technology, 2023. 24: p. 4808-4832; https://doi.org/10.1016/j.jmrt.2023.04.147

[69] Bhattacharjee, R. and S. Chattopadhyaya, Solid State Sciences, 2017. 71: p. 92-110; https://doi.org/10.1016/j.solidstatesciences.2017.06.010

[70] Saleem, S., et al., Investigation of Mn doped BaS for spintronic and thermoelectric applications. 2022. 97(9): p. 095817; https://doi.org/10.1088/1402-4896/ac8a27

[71] Berri, S.J.J.o.S.A.M. and Devices, Ab initio study of fundamental properties of XAlO3 (X= Cs, Rb and K) compounds. 2018. 3(2): p. 254-261; https://doi.org/10.1016/j.jsamd.2018.03.001

[72] Balakrishnan, K., et al., Computational Materials Science, 2025. 246: p. 113439; https://doi.org/10.1016/j.commatsci.2024.113439

[73] Barua, S., et al., Results in Physics, 2022. 42: p. 105973; https://doi.org/10.1016/j.rinp.2022.105973

[74] Munir, J., et al., Spin-polarized electromagnetic and optical response of full-Heusler Co 2 VZ (Z= Al, Be) alloys for spintronic application. 2021. 136: p. 1-18; https://doi.org/10.1140/epjp/s13360-021-01968-x

[75] Xiong, K., J. Robertson, and S.J.A.p.l. Clark, Defect states in the high-dielectric-constant gate oxide LaAlO3. 2006. 89(2); https://doi.org/10.1063/1.2221521

[76] Ambreen, H., et al., Exploring of Be 1-x Cr x Se alloys for spintronics and optoelectronic applications. 2024. 21(4); https://doi.org/10.15251/CL.2024.214.365

[77] Hassan, M., et al., First principles study of electronic structures of Cd0. 9375Co0. 0625X (X= S, Se, Te) for magnetic, optical and thermoelectric device applications. 2018. 238: p. 50-60; https://doi.org/10.1016/j.mseb.2018.12.006

[78] Baaziz, H., et al., FP-LAPW investigations of Zn1-x Bex S, Zn1-x Bex Se and Zn1-x Bex Te ternary alloys. 2006. 243(6): p. 1296-1305; https://doi.org/10.1002/pssb.200541481

[79] Khan, M.A., et al., Comprehensive investigation of Opto-electronic and transport properties of Cs2ScAgX6 (X= Cl, Br, I) for solar cells and thermoelectric applications. 2021. 225: p. 122-128; https://doi.org/10.1016/j.solener.2021.07.026

[80] Batool, A., et al., Applied Surface Science Advances, 2022. 11: p. 100275; https://doi.org/10.1016/j.apsadv.2022.100275

[81] Alias, F.I.H., et al., Journal of Materials Research and Technology, 2022. 18: p. 1623-1630; https://doi.org/10.1016/j.jmrt.2022.03.017

[82] Tariq, M., et al., Solid state communications, 2020. 314: p. 113929; https://doi.org/10.1016/j.ssc.2020.113929

[83] Ahmed, R., et al., Journal of Materials Research and Technology, 2023. 24: p. 4808-4832; https://doi.org/10.1016/j.jmrt.2023.04.147

[84] Ambreen, H., et al., First principle insight on Mn doped BeTe compound for optoelectronic and spintronic applications. 2022. 97(4): p. 045702; https://doi.org/10.1088/1402-4896/ac58cd

[85] Madsen, G.K. and D.J.J.C.P.C. Singh, BoltzTraP. A code for calculating band-structure dependent quantities. 2006. 175(1): p. 67-71; https://doi.org/10.1016/j.cpc.2006.03.007

[86] Fu, Y., et al., Crystals, 2022. 12(10): p. 1406; https://doi.org/10.3390/cryst12101406
[87] Shoukat, L., et al., Journal of Ovonic Research, 2022. 18(5); https://doi.org/10.15251/JOR.2022.185.649